





Enabling S-C-L-Band Systems With Standard C-Band Modulator and Coherent Receiver Using Coherent System Identification and Nonlinear Predistortion

Robert Emmerich , Matheus Sena , Robert Elschner , *Member, IEEE*, Carsten Schmidt-Langhorst, Isaac Sackey , Colja Schubert, and Ronald Freund

(*Top-Scored Paper*)

I. INTRODUCTION

Abstract—One promising and competitive solution to keep up with the rapid growth in data traffic while at the same time addressing increasing network cost, is the efficient reuse of legacy optical fiber infrastructure. This is highly desirable as deployed single mode fibers represent a valuable asset in the network while new installations would require high additional investments. Multiband (MB) or ultra-wideband (UWB) systems, combined with high symbol rates and higher-order modulation formats, are promising solutions to capitalize the already existing fiber plants. In this contribution, we experimentally demonstrate S-C-L-band reception with 64 Gbd dual-polarization (DP) 64-ary and 32-ary quadrature-amplitude modulation (QAM) while using C-band components off-the-shelf (COTS) such as DP-IQ modulators and coherent receivers. To achieve such broadband operation with components that are not optimized for an out-of-band use, mitigation of the associated penalties is decisive. To this end, we apply an end-to-end electro-optical Volterra-based coherent system identification followed by nonlinear digital predistortion of the transmitter. We achieve 150-nm operation bandwidth of the transmission system by performing only a single identification and predistortion at a reference wavelength of 1500 nm.

Index Terms—C-band, fiber optics, L-band, nonlinear filters, optical fiber communication, optical receivers, optical transmitters, S-band, ultra wideband technology, wideband.

Manuscript received July 12, 2021; revised October 1, 2021; accepted October 22, 2021. Date of publication October 27, 2021; date of current version March 2, 2022. This work was supported in part by the German Federal Ministry of Education and Research (Bundesministerium für Bildung und Forschung, BMBF) under the OptiCON Grant 16KIS0990, in part by the the German Research Foundation (Deutsche Forschungsgemeinschaft, DFG) under Grant FR 851/3-1, in part by the EU Horizon 2020 research and innovation program under the MSCA-ETN WON and Grant 814276. (*Corresponding authors: Robert Emmerich.*)

The authors are with the Fraunhofer Institute for Telecommunications Heinrich-Hertz-Institute, 10587 Berlin, Germany (e-mail: robert.emmerich@hhi.fraunhofer.de; matheus.sena@hhi.fraunhofer.de; robert.elschner@hhi.fraunhofer.de; carsten.schmidt-langhorst@hhi.fraunhofer.de; isaac.sackey@hhi.fraunhofer.de; colja.schubert@hhi.fraunhofer.de; ronald.freund@hhi.fraunhofer.de).

Color versions of one or more figures in this article are available at <https://doi.org/10.1109/JLT.2021.3123430>.

Digital Object Identifier 10.1109/JLT.2021.3123430

THE constant reduction of network cost in the context of the continuing rapid growth in data traffic is a priority for operators in order to prevent the forthcoming cost-per-bit crunch. In this context, the global COVID-19 pandemic in 2020/2021 emphasized the critical role of digital global networks that fully rely on the underlying optical infrastructure. Virtual private network (VPN) and video conferencing traffic for remote working has increased beyond 200% during the pandemic [1]. Since workday traffic patterns are changing quickly, the pressure on the existing network infrastructure is further growing. These developments as well as the forthcoming capacity crunch, are one of the priority concerns for operators and require innovative approaches to increase the achievable capacity. This increases the need for an efficient reuse of already deployed optical fiber infrastructures, as these represent a valuable asset in optical transmission systems [2]–[4]. In line with this goal, multiband (MB) or ultra-wideband (UWB) dense wavelength division multiplexing (DWDM) transmission, in combination with high symbol rates and high-order modulation formats, are an extremely promising solution to increase the capacity. Applying high symbol rates in a MB system can reduce the amount of transponders. Adding the currently introduced long wavelength band (L-band) [5]–[8] to the conventional band (C-band) increases the available bandwidth by 60 nm (~ 7.1 THz) and allows for up to 95 nm (~ 11.5 THz) of total bandwidth. However, extending transmission beyond the L-band as a near- to short-term solution is seen as a key enabler towards cost-effective capacity upgrades of commercial optical systems. For that, the next step as a mid-term solution is to unlock the benefits of other transmission bands such as the short wavelength band (S-band) to further increase the available capacity of the already deployed single mode fiber (SMF) and enable optical networks to adapt to the highly dynamic traffic patterns. For such a SMF capacity increase, the combination of S-C-L-band offers the highest bandwidth while still operating within the minimum loss regime of the transmission fiber. Here, the S-band can add

additional 70 nm (~ 9.4 THz) and enables a total combined bandwidth of 165 nm (~ 20.9 THz).

In this contribution we extend our previous experimental work [9] by including a new section to further describe the applied end-to-end electro-optical Volterra-based coherent system identification (SI). We also incorporate in our analysis additional insertion loss measurements of the used C-band modulator and characterize the responsivity of the coherent receiver over the S-C-L-band. In order to quantify the impact of the used doped fiber amplifiers we added as well noise figure measurements for each band. To further understand the performance in the S-band, we include the spectra of the investigated signal at different wavelengths and measurement points in the setup.

Recently, experimental research of MB systems with S-C-L-band transmission over SMF for high capacity systems has gained substantial attention in the community. Today, such systems rely on non-commercial prototypes for amplification such as broadband semiconductor optical amplifiers (SOA) [10] or a combination of Erbium-doped fiber amplifier (EDFA) for the C+L-band with distributed Raman amplification for the S-band [11]. With the accessibility of commercially available Thulium-doped fiber amplifiers (TDFAs) for the S-band, further solutions that combined EDFAs and TDFAs with either discrete Raman [12] or distributed Raman amplification [13] have been demonstrated. To further overcome performance limitations in the S-band different solutions including probabilistically shaped (PS) 64-QAM [10], lower channel symbol rates [11], [13] or customized wavelength-dependent modulation formats such as geometrically shaped (GS) constellations [12] are used. Currently, due to unavailability of commercial S-band transponders, the only option is to use standard C-band components-off the shelf (COTS) such as modulators and coherent receivers. However, these components are not optimized for an out-of-band use. In order to transmit high symbol rates while using conventional higher-order QAM modulation formats without non-commercial Raman or SOA amplification in the S-band, mitigation of the associated penalties will be essential to achieve similar performance as in the designed target wavelength band.

In this contribution, we experimentally characterize the wavelength-dependent degradation of an MB optical transmission system and study the feasibility of an S-C-L-band transmission by wavelength-tuning of a single channel in a back-to-back (b2b) scenario. We investigate the system performance at a symbol rate of 64 GBd with dual-polarization (DP) 64- and 32-QAM (further called 64-/32-QAM), by utilizing standard C-band COTS. Here a commercially available Lithium Niobate (LiNbO_3) DP in-phase and quadrature (IQ) modulator and a phase- and polarization-diversity free-space 90° optical hybrid, as part of the coherent receiver, are used. The performance in the S-C-L-band is evaluated regardless of the used modulation format by characterizing the full end-to-end channel. This includes the optical modulator, optical and electrical amplifiers, and the optical receiver. Furthermore, all required electronics such as digital-to-analog converters (DAC) and analog-to-digital converters (ADC) and the digital signal processing (DSP) at the

transmitter and the receiver sides are included in the investigated end-to-end channel. To quantify the system performance, metrics such as the effective end-to-end signal-to-noise ratio (SNR_{eff}) [14] and the bit-error ratio (BER) at the input of the decision circuitry are used. Since the transmission system is fully characterized, the performance can be further improved for out-of-band use by employing higher RF-power into the modulator, thus increasing the optical output power, and applying the concept of nonlinear digital predistortion (NLPD) [15] to overcome the introduced nonlinearities in the transmitter. The higher output power can directly be translated to an increase in SNR_{eff} and an reduction in the noise figure for optical amplifiers. The SI consists of modeling the optical transmitter as a truncated, time-invariant Volterra series, which permits the NLPD to derive an inverse filter that compensates for component-induced distortions. This can be used to identify and mitigate distortions, i.e., reduce the optical signal-to-noise-ratio (OSNR) penalty and hence allow for standard C-band modulators and coherent receivers to be used in unconventional bands. For that, a single NLPD that is based on a SI at 1500 nm will be applied in this work. Thus, the same modulation format and predistortion filter (that is based on one set of kernel coefficients) can be used across all wavelengths. This is based on results presented in [16] where no significant gain in achievable Q^2 factor was obtained by performing SI and NLPD per-wavelength for each investigated channel. A single SI and NLPD, as used in this work, reduces the characterization effort and computational complexity since the same filter kernel coefficients can be applied across all wavelengths for a MB/UWB system in contrast to an autonomous digital predistortion scheme for multiband as shown in [17], a custom PS-QAM in [10] or per wavelength optimizations and custom GS constellation formats as in [12]. We employ an end-to-end Volterra-based coherent SI method to characterize the full end-to-end transmission system, as described in [18] and combine it with the NLPD scheme reported in [24]. With that, we achieved a usable bandwidth of ~ 150 nm for 32-QAM and ~ 140 nm for the 64-QAM signals at a BER below the soft-decision forward-error correction (SD-FEC) threshold (at $2 * 10^{-2}$) in a b2b configuration. In comparison to the application of only linear predistortion, an order-of-magnitude BER reduction (1.59 dB in Q^2) is achieved for the 32-QAM signal with the nonlinear predistortion scheme at a wavelength of 1500 nm. Furthermore, an improvement up to 1.2 dB in SNR_{eff} for the 32-QAM and the 64-QAM signals were measured.

The remainder of this paper is structured as follows. The used end-to-end Volterra-based coherent system identification including the applied experimental setup and further details on the applied DSP are provided in Section II. The experimental setup for the system performance evaluation in the S-C-L-band is provided and explained in Section III. As part of the experimental results and discussion in Section IV, b2b characterizations are provided in the S-band at 1500 nm as well as in the C-band at 1550 nm as a reference point for the originally intended wavelength of the system. Here, the performance of the linear and the nonlinear predistortion are compared and discussed. Furthermore, the performance of a single channel

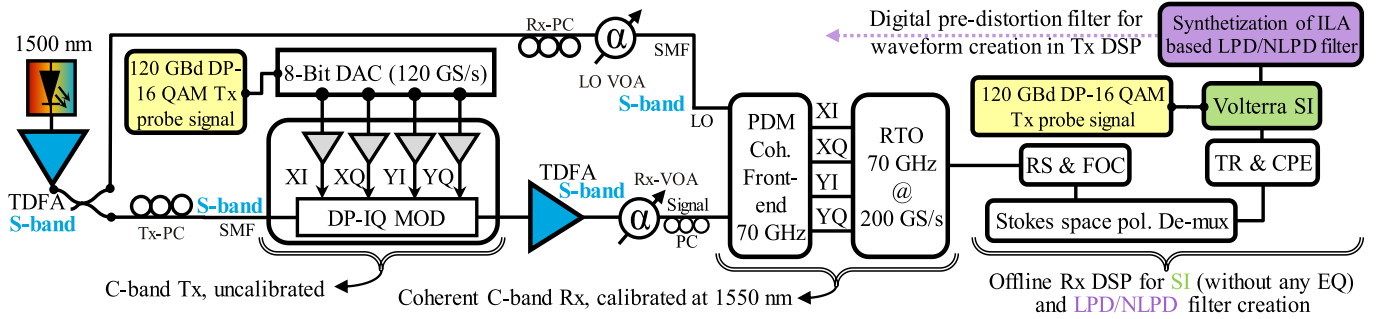


Fig. 1. Experimental setup and the offline Rx DSP for the Volterra based end-to-end coherent system identification (SI, green) in the S-band, including the linear or nonlinear digital predistortion (LPD, NLPD, purple) block that is based on an indirect learning architecture (ILA). Both pre-distortion filters enable the creation of the waveforms for later performance assessment. TDFA: Thulium-Doped Fiber Amplifier. Tx/Rx: Transmitter/Receiver. DSP: Digital Signal Processing. PC: Polarization Controller. DAC: Digital-to-Analog Converter. VOA: Variable Optical Attenuator. LO: Local Oscillator. RTO: Real Time Oscilloscope. RS: Resampling. FOC: Frequency Offset Correction. TR: Timing Recovery. CPE: Carrier Phase Estimation. EQ: Equalization.

in the investigated b2b scenario at maximum OSNR over the full S-C-L-band is measured and compared between 32- and 64-QAM while applying NLPD. In addition to the performance characterization, measurements of the TDFA and EDFA noise figures in the S-C-L-band are added. The individual component characterizations of the modulator and the coherent receiver as well as signal spectra in the S-band are presented in Section V. At last, the main conclusions and considerations are drawn in Section VI.

II. END-TO-END COHERENT SYSTEM IDENTIFICATION

In order to characterize the distortions induced by the out-of-band use of the C-band COTS, we employed an end-to-end coherent SI as reported in [18]. To compensate the transmitter impairments from a full end to end SI, by the means of predistortion, we removed as a first step the static distortions purely originated from IQ skew, 90° phase error, IQ imbalance and frequency response induced by the optical coherent receiver frontend (CRF) and the real time oscilloscope (RTO). For that, we performed an offline receiver calibration at 1550.116 nm (193.4 THz) assuming a calibrated C-Band receiver would be available in a potential future multiband transmission system. For that, one continuous wave (CW) from an external cavity lasers (ECL) is launched into the local oscillator (LO) input and one CW into the signal input. They are used to measure the transfer function and the 90° phase error of the coherent receiver over ± 70 GHz (in ref. to 193.4 THz) by tuning the signal CW accordingly. The derived results are used to compensate the above mentioned impairment of the receiver after each signal acquisition. This is done for all following identification as well as later performance measurements, in the receiver DSP to create a calibrated coherent C-band receiver.

The experimental setup that is used as second step for the end-to-end electro-optical Volterra-based coherent SI in the S-band at 1500 nm is shown in Fig. 1. This wavelength in the center of the S-band is selected according to the results in [16]. We performed an identification of the full transmission system in the S-band with a DAC operated at 120 GS/s with a 3 dB

bandwidth of up to 45 GHz. The 120 GBd DP-16-QAM probe signal (yellow box in Fig. 1) was generated using a 2^{15} random bit sequence at one sample per symbol (i.e., no pulse shaping was applied). The 120 GBd probe signal does not include any predistortion and ensures that the identification of the transmitter (i.e., the later derived Volterra model) covers sufficient frequency components to guarantee that no restriction in the frequency domain is present and further head room for a later symbol rate increase is available. Since the probe signal for the SI needs to excite multiple DAC levels, a modulation format with a high cardinality is required. However, impairments of the signal will limit the maximum usable cardinality and a DP-16-QAM signal at 120 GBd is an ideal format for a probe signal, since it is more resilient to impairments when compared to higher cardinalities. Further details regarding the experimental setup and the used optical equipment to generate and capture the probe signal are provided in Section III. After signal acquisition the receiver impairments are compensated and the signal is passed to the offline Rx DSP as shown in the right hand part of Fig. 1. To measure the nonlinear system distortions independently for each quadrature and polarization, the four received quadrature's (XI, XQ, YI, YQ) of the optical probe signal must be separated in the DSP without any equalization. As a first step, the distorted probe signal is resampled (RS) to two samples per symbols (SPS) and the frequency offset is removed [19] (if needed). Following that, a blind single-tap polarization de-multiplexing based on a Stokes-space approach [20] is performed. In order to synchronize the transmitted and received waveforms a timing recovery (TR, i.e., a clock phase recovery) is performed. In order to de-couple the IQ components, the phase noise is removed by a 'genie' carrier phase estimation (CPE) with full knowledge on the transmitted sequence [21]. The received and normalized signal, as well as the transmitted samples of the 120 GBd DP-16-QAM probe signal (yellow box at the right side in Fig. 1), are finally provided to the Volterra SI block (green box within Fig. 1). To identify the experimental setup, a truncated and time-invariant, third-order Volterra series with memory lengths of 512, 20, 20 taps, as used in [18], is derived. These kernels are obtained with a least square estimation [22]

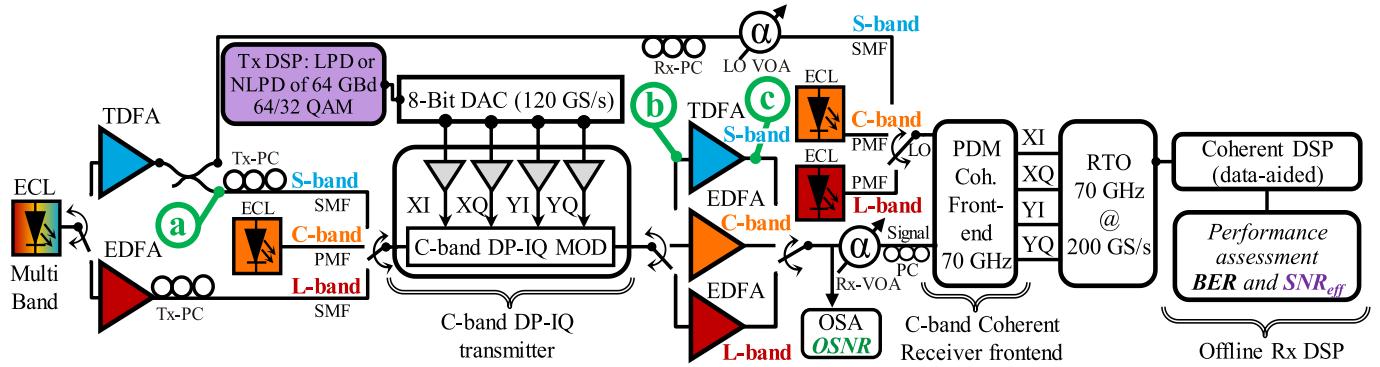


Fig. 2. Experimental setup used for multiband back-to-back (b2b) characterization of BER, OSNR and SNR_{eff} vs. wavelength. Green letters (a-c) represent the measurement points for signal spectra (see Fig. 7). ECL: External Cavity Laser. Tx/Rx: Transmitter/Receiver. PC: Polarization Controller. PMF: Polarization Maintaining Fiber. SMF: Single Mode Fiber. VOA: Variable Optical Attenuator. LO: Local Oscillator. OSA: Optical Spectrum Analyzer. RTO: Real Time Oscilloscope.

and describe the linear as well as the nonlinear distortions of the transmission system for each quadrature individually. Following the SI, a predistortion filter (purple box in Fig. 1) is synthesized for up to 96 GBd using an indirect-learning architecture (ILA) [23]. The filter is applied for performance evaluation in Section III and IV in order to assess the ability to mitigate the nonlinearities caused by the system including additional penalty caused by the out-of-band use. For the NLPD of the identified system, a filter with a kernel memory lengths of 512, 9, 9 taps, as proposed in [18], is created. This enabled the mitigation of the linear frequency response including skew of the system and of the wavelength independent nonlinear transfer characteristics, in particular, of the sinusoidal modulator, and of the nonlinear DAC and driver amplifier (DA). The used ILA and the applied NLPD scheme are further explained in [24]. As already described earlier in Section I, the SI and NLPD results obtained at 1500 nm (i.e., the derived digital predistortion filter for waveform creation in the Tx DSP) are applied to transmit data at all investigated wavelengths across the S-C-L-band. This reduces the computational complexity since the same filter kernel coefficients can be applied across all wavelengths in a MB/UWB system, thus avoiding multiple regressions of the least-square method.

III. EXPERIMENTAL SETUP FOR SYSTEM EVALUATION

The experimental setup used to evaluate the system performance is shown in Fig. 2. The 64 GBd 64/32-QAM signals for the S-C-L-band are all generated using a single commercially available C-band $LiNbO_3$ DP-IQ modulator. An ECL with $P_{out} = 0$ dBm and <100 kHz linewidth is amplified in front of the modulator to 16 dBm by a TDFA for the S-band EDFA for the L-band while the C-band signal is directly created from a separate ECL ($P_{out} = 16$ dBm, <100 kHz linewidth). The setup covers wavelength ranges of 1460-1530 nm, 1528-1562 nm and 1560-1608.8 nm, covering the S-C-L-band. A 120-GS/s, 8-bit, 4 channel DAC is used to drive the modulator via four linear driver amplifiers (DA). The end-to-end electro-optical Volterra-based coherent SI is performed only once at 1500 nm. From that SI,

Volterra kernels up to third order are derived to describe all linear and nonlinear distortions of the system as already described in Section II. The created transmitter waveforms include data-aided header and Nyquist pulse shaping with a root-raised cosine (0.1 roll-off). Following that, a NLPD filter is created with a kernel memory length of 512, 9, 9 taps, as investigated in [18] using the concept in [24], to mitigate the sinusoidal modulator and the nonlinear DAC/DA transfer characteristic. In order to compare the NLPD filter with a pure linear digital predistortion (LPD), we created an LPD filter that is based on the same setup (i.e., SI) using only first order Volterra kernels with 512 taps memory to compensate only for the linear frequency responses. These waveforms are used for all wavelengths. At the receiver, per band amplification based on a TDFA for the S-band and individual EDFAs for the C- and the L-band are used. In case of the BER and SNR_{eff} vs. OSNR characterization (Fig. 3) an additional variable optical attenuator (VOA) in front of the receiver amplifier stage is used to perform a variation of the OSNR by noise loading. The OSNR is measured at the output of that amplification stage and the signal is mixed with the local oscillator (LO) in the 70 GHz CRF comprising a free-space 90° optical hybrid. For C-L-band, two separate ECLs are used as LO to perform intradyne coherent reception. In case of the S-band, the ECL in front of the transmitter is splitted and 25% of the light is used as LO to enable a self-homodyne coherent reception to overcome the lack of a second S-band ECL. The outputs of the CRF are subsequently digitized at a sampling rate of 200 GS/s using a four channel RTO with 70 GHz analog electrical bandwidth. The offline DSP at the receiver includes optical frontend corrections (based on 1550 nm calibration), resampling to two SPS, data-aided carrier-frequency offset compensation and equalization [25], as well as a blind phase search for carrier phase estimation (CPE). This is followed by a real-valued 4×4 multiple-input and multiple-output time-domain equalizer (with 15 taps, T-spaced) adaption based on a decision directed least-mean square (DDLMS) criterion to compensate for residual modulator I/Q imbalances and phase errors [26]. As with the block length of the CPE, the used step-size (μ) of the DDLMS equalizer is optimized to minimize the BER values by a brute

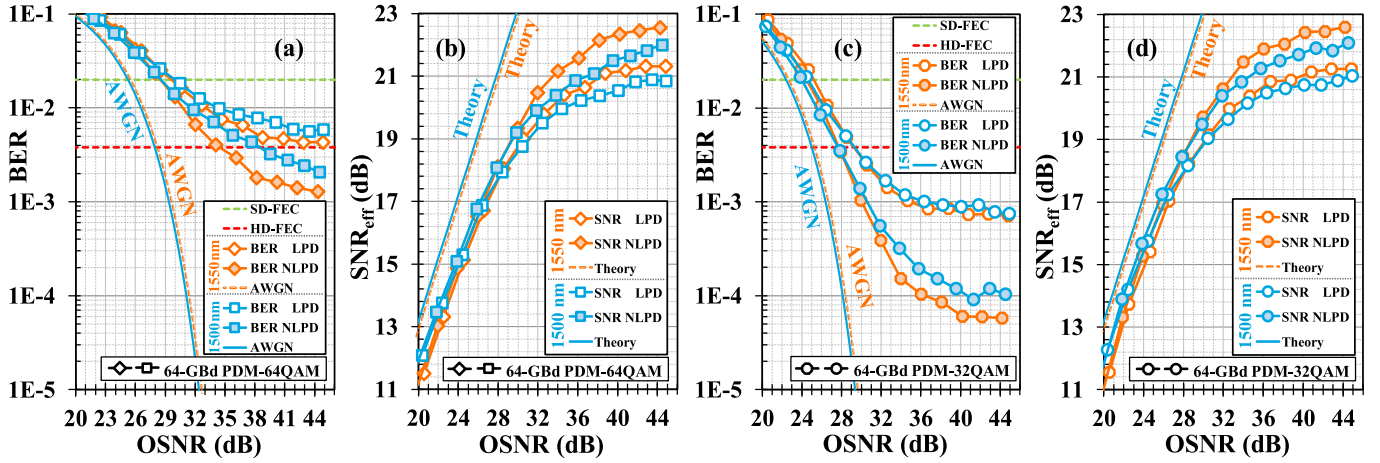


Fig. 3. (a) B2b BER and (b) SNR_{eff} for 64 GbD PDM-64 QAM (square and diamond symbols), (c) B2b BER and (d) SNR_{eff} for 64 GbD PDM-32-QAM (circle and octagon symbols). Plotted versus the OSNR (in 0.1 nm) for linear predistortion (PD) (hollow symbols) and nonlinear PD (filled symbols) at 1500 nm (S-band, blue) and 1550 nm (C-band, orange) including the corresponding wavelength dependent AWGN and SNR_{eff} theory values as well as the SD- / HD-FEC limits.

force search per wavelength to ensure ideal performance of the receiver DSP. Finally, the SNR_{eff} and the pre-FEC BER at the decision circuit are calculated after symbol-to-bit demapping by processing of at least 5 million bits per wavelength.

IV. EXPERIMENTAL RESULTS AND DISCUSSION

Fig. 3(a), (c) provides the BER result of the b2b characterization for 1500 and 1550 nm with LPD and NLPD for 64-QAM and 32-QAM signals as a function of the OSNR. The wavelength dependent additive white Gaussian noise (AWGN) curves and the used SD-FEC (2×10^{-2}) and hard-decision-FEC (HD-FEC, 3.8×10^{-3}) thresholds are included. For 64-QAM in Fig. 3(a) at 1500 nm (blue), we observe an error floor at a BER of 6×10^{-3} for LPD (hollow square symbols) which can be improved to 2×10^{-3} with NLPD (filled square symbols) at the maximum OSNR of 44.5 dB. This allows the reception with a BER below the HD-FEC threshold at around 38.5 dB OSNR. The corresponding curves for 1550 nm (orange), are added as reference for the designed target performance in the C-band and yield a BER of 1.3×10^{-3} with NLPD (filled diamond symbols) at 44.3 dB OSNR. Please note that the maximum OSNR in the C-band is 48 dB. However, due to the error floor, no significant BER improvement is observed at an OSNR higher than 44 dB. The OSNR in the S-band is limited by the higher noise figure of the TDFA (see as well Fig. 6) and the transmitter laser setup. In the case of 32-QAM at 1500 nm (blue curves with circles) in Fig. 3(c) a maximum BER improvement from $\sim 9 \times 10^{-4}$ to $\sim 9 \times 10^{-5}$ (Q^2 improvement of 1.59 dB) can be achieved with NLPD at 41 dB OSNR, that is reduced to 1.35 dB in Q^2 for maximum OSNR. Fig. 3(b), (d) shows the measured SNR_{eff} (estimated at the soft-demapper input assuming circularly symmetric Gaussian distributed noise) and the wavelength dependent AWGN theory vs. OSNR for 64- and 32-QAM, respectively. Both modulation formats saturate at the maximum available SNR_{eff} that is limited by the transmitter and the receiver components as well as the wavelength. At low

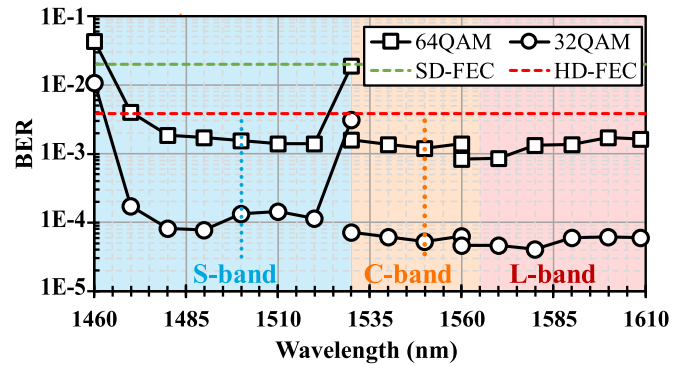


Fig. 4. B2b BER for 64 GbD DP-64/32-QAM as a function of the wavelength for S-C-L-band measurements. All results are based on NLPD, the reference wavelengths (1500 nm blue and 1550 nm orange horizontal dotted lines) from the BER vs. OSNR characterization are included.

OSNR values, 64- and 32-QAM approach their theory curves per wavelength, offset by the implementation penalty. Applying the proposed single identification and predistortion at the reference wavelength of 1500 nm to both investigated wavelengths, an improvement of up to 1.2 dB in SNR_{eff} for the NLPD (filled symbols), compared to the LDP (hollow symbols), can be realized as shown in Fig. 3(b), (d). This findings substantiate the discussed BER improvements in Fig. 3(a), (c). At this wavelength in the S-band, 64- and 32-QAM reach a similar SNR_{eff} performance at high OSNR with only minor deviation for reduced OSNR. Comparing the SNR_{eff} results for NLPD (filled symbols) at 1500 nm with 1550 nm in Fig. 3(b), (d), a delta of ~ 0.5 dB for both formats at 44.2 dB OSNR is present. Here the S-band performed worse compared to the C-band. These results are in contrast to the expectation considering the difference given by the theory curves, with a delta of -0.285 dB, were the S-band performs better compared to the C-band. The penalties in the S-band are attributed to residual impairments, such as splitting ratio mismatch (resulting in a reduced extinction ratio of the

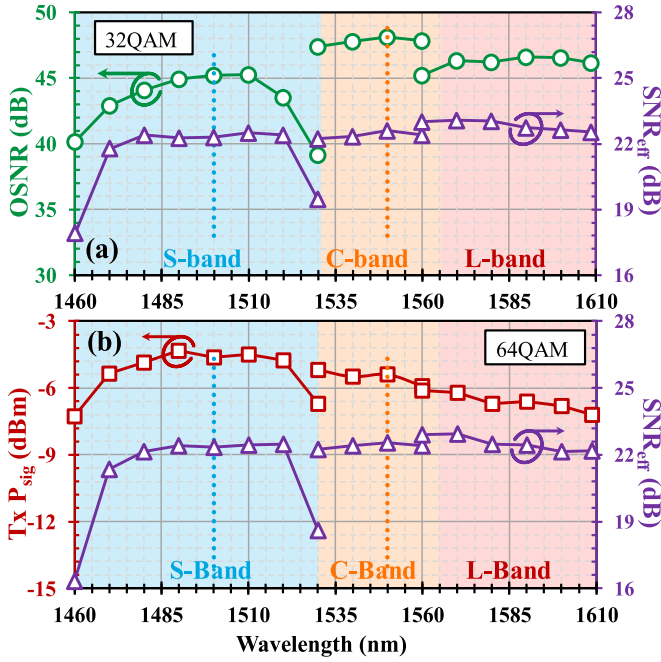


Fig. 5. (a) Maximum OSNR (in 0.1 nm) and SNR_{eff} for DP-32-QAM and (b) transmitter output power as well as SNR_{eff} for DP-64-QAM. All points are plotted as a function of wavelength for the S-C-L-band measurements.

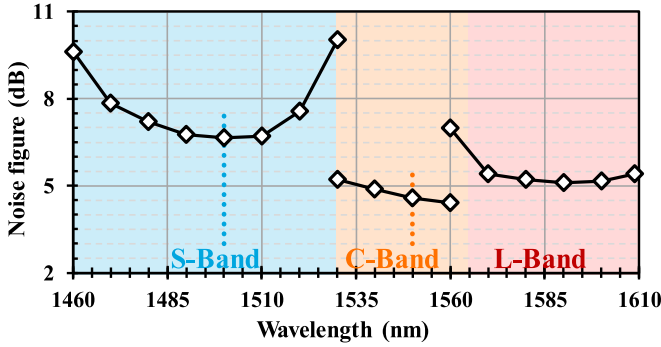


Fig. 6. Noise figure for the three S-C-L-Band amplifiers as a function of the wavelength based on the individual transmitter output power (see of Fig. 5(b) Tx P_{sig}) of each channel under test. Amplifiers under investigation are shown in Fig. 2 between the green letters b and c.

Mach-Zehnders) and 90° phase error (between I and Q) caused by the C-band modulator. Additionally, amplitude imbalance, skew difference, and 90° phase errors of the coherent receiver may not corrected completely and degrade the performance in the S-band further. The residual impairments of the modulator and the receiver cannot be compensated completely by the applied nonlinear predistortion. The wavelength dependent theory curves for SNR_{eff} in dB as a function of the OSNR are calculated as follows:

$$SNR_{eff} [dB] = 10 * \log_{10} \left(\frac{OSNR [lin] * \Delta f [GHz]}{symbol\ rate [GHz]} \right) \quad (1)$$

where $OSNR[lin]$ is the linear value of the corresponding OSNR that is multiplied with the wavelength depend $(\Delta) f$ value in GHz. The *symbol rate* in GHz is fixed to 64 in this experiment. Delta f at 1550 nm is 12.476 GHz and at 1500 nm it is 13.321 GHz, this is based on the relation at 1548.515 nm (193.6 GHz) where Δf is 12.5 GHz (0.1 nm) as defined in [27].

Fig. 4 shows the results for the BER vs. wavelength characterization at a spacing of 10 nm starting from 1460 nm up to 1608.8 nm. Here, the same SI and NLPD, based on the fixed wavelength of 1500 nm, were used for all bands. As shown in Fig. 4, 32-QAM signals (circles) can be received from 1460 nm up to 1608.8 nm, while 64-QAM (squares) can only be received from 1470 nm to 1608.8 nm, with a BER below the SD-FEC. For both formats, the achievable BER in the L-band is comparable to the C-band, with negligible differences. For S-band signals at 1460 nm as well as 1530 nm, a penalty is observed that results in a severe performance degradation. This is caused by the limited per-channel output power and the increased out-of-band noise of the TDFA at these points (as shown in Fig. 7). This degradation is confirmed in the corresponding OSNR data in Fig. 5(a). The maximum achievable OSNR (green-border circles) and the SNR_{eff} (purple triangles) for 32-QAM are shown in Fig. 5(a) over the same wavelength range. The OSNR values for 64-QAM are not plotted, however the data of 32-QAM can be used for 64-QAM in good approximation (deviation in OSNR below 0.1 dB). Comparing the achievable SNR_{eff} (purple-border triangles) for 32-QAM in Fig. 5(a) with the values for 64-QAM in Fig. 5(b), only minor variations, typically below 0.3 dB, are present. The output power (red-border square symbols) out of the modulator for 64-QAM is provided in Fig. 5(b). The values for 64-QAM apply as well for 32-QAM. The output power reduction for the highest and the lowest wavelength (i.e., 1460 nm and 1530 nm) in the S-band is further confirmed by Fig. 7(b). For the L-band in Fig. 5(b) we observe a reduction in transmitter output power for higher wavelength that is caused by the non-ideal Tx laser setup as shown in Fig. 2. However, the OSNR in the L-band is not affected by this reduction. Since the BER in the L-band did increase for higher wavelength, the reason must be the receiver as show in Section V. Please note, that all OSNR values are measured for a noise power density referred to 0.1 nm (equal to 12.5 GHz) at 1548.515 nm (193.6 THz). This is subsequently corrected for wavelength dependency according to [27]. The wavelength dependent OSNR correction can be expressed as:

$$OSNR_f [dB] = OSNR_{193.6\ THz} - 20 * \log_{10} \left(\frac{f [THz]}{193.6\ THz} \right) \quad (2)$$

here the $OSNR_f$ in dB at the measurement frequency f is equal to the $OSNR$ obtained at 193.6 THz minus the logarithmic value of the ratio between the measurement frequency f in THz and 193.6 THz. To further quantify the impact of the used doped fiber amplifiers on the system performance and the achievable OSNR, Fig. 6 summarizes the NF for each amplifier at the output of the modulator. Here the increased NF in the S-band, compared to C- and L-band, is evident.

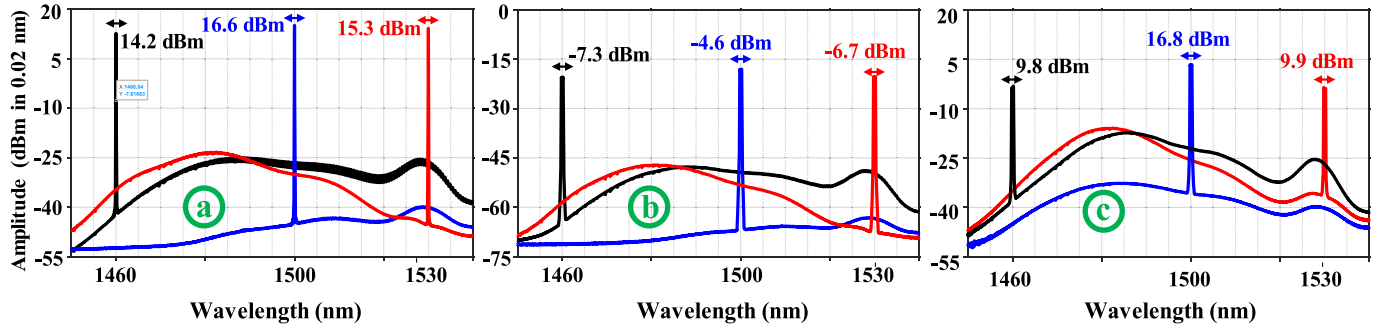


Fig. 7. S-Band signal spectra including channel power (excluding out-of-band noise) for 1460 nm, 1500 nm and 1530 nm according to measurements points in the experimental setup (see green letters in Fig. 2). (a) Shows the amplified laser spectrum at the input of the modulator. (b) The modulated signal at the output of the modulator. (c) Represents the signal spectrum at the input of the coherent receiver before attenuation.

Finally the 3 different plots shown in Fig. 7(a)–(c) represent the individual measured spectra for 1460, 1500 and 1530 nm in the S-band at the points that are highlighted by green letters in the experimental setup (Fig. 2). The input signal into the modulator is plotted in Fig. 7(a) and consists of the CW from the multiband ECL that is amplified by the first TDFA. This signal is also used as LO for the CRF, although with less power due to the 25/75 % coupler after the TDFA. Here the OSNR degradation/limitation caused by the additional amplifier after the ECL is especially visible at 1460 and 1530 nm. This is also confirmed by the reduction of channel power compared to 1500 nm. Fig. 7(b) represents the modulated signal at the output of the transmitter. The reduction in total power per channel is caused by the intrinsic insertion loss (IL) as well as the modulation induced loss (dependent on RF-power) of the modulator. The delta between Fig. 7(a) and (b) is equal to the wavelength depend loss of the transmitter as shown for S-C-L-band in Fig. 8(a). After the transmitter, a second TDFA is used to boost the signal power in front of the coherent receiver. This amplifier changes the power distribution over wavelength as shown in Fig. 7(c). Comparing 1460 nm and 1530 nm with 1500 nm does further explain the BER increase at these two wavelengths in Fig. 4. This is purely caused by the used S-band TDFA rather than by the NLPD processing. The per channel power delta (i.e., the gain ripple of the amplifier) in this case is in the order of 7 dB (i.e., 9.8 dBm and 9.9 dBm to 16.8 dBm). The root cause for this degradation is the increase in out-of-band noise of the TDFA that did reduce the power at the target wavelengths. For 1530 nm a C-band EDFA is the logical choice as already shown in Fig. 4. However, at this point in time no alternative amplification for 1460 nm is commercially available and the performance degradation limits the usability of the system at this wavelength.

V. MODULATOR AND COHERENT RECEIVER MEASUREMENTS

In order to further explain the measured performance for the investigated COTS within a multiband use case, additional characterizations of the modulator and the coherent receiver are performed. The total combined insertion loss of the used LiNbO₃ modulator within the transmitter is given in Fig. 8(a) by the square hollow symbols over the investigated wavelength range.

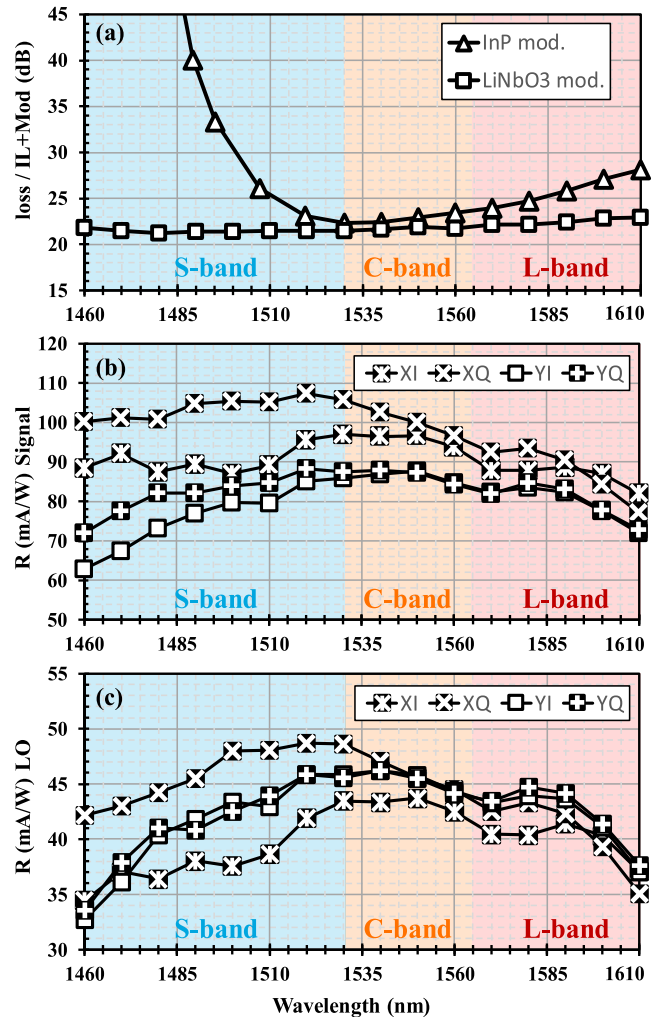


Fig. 8. Insertion and modulation induced loss (a) of the transmitter and responsivity for the LO-path (b) and the signal-path (c) for the coherent receiver. All points are plotted as a function of wavelength for the S-C-L-band measurements.

The plotted loss on the y-axis did include the component based IL as well as the loss that is caused by driving the modulator with a limited RF-signal, this is also referred to as modulation induced loss. In order to measure this parameter, a multiband

ECL was used and the output power profile was calibrated. The drive signal into the modulator was set to 64 GBd 64-QAM. The loss values at 1460, 1500 and 1530 nm can be extracted as well in good approximation from the delta in power level provided in Fig. 7(a) and (b). Over all the LiNbO₃ modulator shows a relative flat frequency dependence and hence can be used for a multiband system with only minor penalties in the L-Band that can easily be overcome by optical amplification. For comparisons, we added measurements of an InP based DP-IQ modulator (from ID-Photonics). The results are included in Fig. 8(a) as hollow triangles symbols. For that modulator we observe a strong wavelength dependence with slight increased loss in the L-band and a strong increase within the S-band. This results in a C/L-band only use case for this modulator type, since the loss in the S-band is too severe to be compensated by amplification.

To complete the measured system performance investigations, we summarized the characterization of the coherent receiver by plotting the responsivity (R), of the signal- and the LO-path, as a function of wavelength in Fig. 8(b), (c) for all four outputs. The same multiband ECL with a calibrated output power profile was used for individual measurements of the signal and the LO input. For both input ports, the ideal performance is observed in the C- and the higher S-band (1500–1565 nm), while the R in the L-band is further reduced at wavelength above 1585 nm. The same behavior is present in the S-band below 1500 nm, and can be worse compared to the L-band below 1480 nm. Additionally, in the lower S-band wavelength range we observe a polarization dependence such that the responsivity of the Y-polarization (hollow square and plus square symbols in Fig. 8(b), (c)) is further reduced compared to the X-polarization. To overcome the limitation in the S- and the L-band the power into the coherent receiver can be optimized per wavelength as done for the system performance measurements with the Rx-VOA in Fig. 2. In case of the lower wavelengths in the S-band, this is not possible since the amplified power per channel out of the TDFA is not big enough (see Fig. 7(c)) to overcome the drop in R. This does directly result in a limited swing on the RTO and would cause further penalties if the ADC scaling factor were not adjusted accordingly.

VI. CONCLUSION

We investigated the feasibility of using standard C-band modulators and coherent receiver in the S-C-L-band with 64 GBd dual-polarization- (DP) 64-QAM and DP-32-QAM signals by performing a single end-to-end electro-optical Volterra-based coherent system identification (SI) at 1500 nm and applying the same nonlinear digital predistortion (NLPD) for all investigated wavelengths. Since the transmission system is fully identified by the SI, an increased RF-power into the modulator can be utilized to reduce the optical signal-to-noise-ratio penalty while the added distortions are mitigated by the NLPD. It was shown that DP-64-QAM can be received over 140 nm, while DP-32-QAM can support up to 150 nm bandwidth with a bit-error ratio below the hard-decision forward-error correction threshold. This enables transmission with up to 600 Gb/s net

data rate per channel in the unconventional S-band as well as in the C- and in the L-band. The SI and NLPD at 1500 nm yielded an improvement in BER by an order-of-magnitude (from $\sim 9 * 10^{-4}$ to $\sim 9 * 10^{-5}$) for DP-32-QAM compared to pure linear predistortion. By adding the S-band for transmission, a large increase of the usable bandwidth of the single mode fiber (beyond a C/L-multiband system) is supported with standard C-band modulators and coherent receivers while using commercially available thulium-doped fiber amplifiers and conventional higher-order QAM modulation.

ACKNOWLEDGMENT

The authors would like to thank Dr. M. Sezer Erkılınc for his support and the fruitful discussions during the experiment and the preparation of the manuscript, as well as ID-Photonics for the InP DP-IQ modulator.

REFERENCES

- [1] A. Feldmann *et al.*, "The lockdown effect: Implications of the COVID-19 pandemic on internet traffic," in *Proc. AMC Internet Meas. Conf.*, Virtual Event, Oct. 2020, pp. 1–20, doi: [10.1145/3419394.3423658](https://doi.org/10.1145/3419394.3423658).
- [2] J. K. Fischer *et al.*, "Maximizing the capacity of installed optical fiber infrastructure via wideband transmission," in *Proc. Int. Conf. Transparent Opt. Netw.*, Bucharest, Romania, Jul. 2018, pp. 1–4, Paper Tu.B3.3, doi: [10.1109/ICTON.2018.8473994](https://doi.org/10.1109/ICTON.2018.8473994).
- [3] R. Emmerich *et al.*, "On the prospects of multi-band WDM transmission," in *Proc. IEEE Asia Commun. Photon. Conf.*, Hangzhou, China, Oct. 2018, pp. 1–20, doi: [10.5281/zenodo.3937668](https://doi.org/10.5281/zenodo.3937668).
- [4] A. Ferrari *et al.*, "Assessment on the achievable throughput of multi-band ITU-T G.652.D fiber transmission systems," *J. Lightw. Technol.*, vol. 38, no. 16, pp. 4279–4291, Aug. 2020, doi: [10.1109/JLT.2020.2989620](https://doi.org/10.1109/JLT.2020.2989620).
- [5] A. K. Srivastava *et al.*, "Ultradense WDM transmission in L-band," *IEEE Photon. Technol. Lett.*, vol. 12, no. 11, pp. 1570–1572, Nov. 2000, doi: [10.1109/68.887758](https://doi.org/10.1109/68.887758).
- [6] F. Paolucci *et al.*, "Filterless optical WDM metro networks exploiting C+L band," in *Proc. IEEE Eur. Conf. Opt. Commun.*, Rome, Italy, Sep. 2018, pp. 1–3, Paper Tu.1.D.5, doi: [10.1109/ECOC.2018.8535529](https://doi.org/10.1109/ECOC.2018.8535529).
- [7] R. Emmerich *et al.*, "Dual-Band node architectures for C+L-Band capacity upgrades in optical metro transport networks," in *Proc. VDE Photon. Netw.; 21th ITG-Symp.*, ITG-Fb. 294: Photonische Netze, Nov. 2020, pp. 14–19, [Online]. Available: ieeexplore.ieee.org/document/9273685
- [8] V. Lopez *et al.*, "Optimized design and challenges for C&L band optical line systems," *J. Lightw. Technol.*, vol. 38, no. 5, pp. 1080–1091, Mar. 2020, doi: [10.1109/JLT.2020.2968225](https://doi.org/10.1109/JLT.2020.2968225).
- [9] R. Emmerich *et al.*, "Enabling S-C-L-band systems with standard C-band modulator and coherent receiver using nonlinear predistortion," in *Proc. IEEE/OSA Opt. Fiber Commun. Conf. Exhib.*, Jun. 2021, pp. 1–3, Paper F4D.7, [Online]. Available: ieeexplore.ieee.org/document/9489930
- [10] J. Renaudier *et al.*, "First 100-nm continuous-band WDM transmission system with 115 Tb/s transport over 100 km using novel ultra-wideband semiconductor optical amplifiers," in *Proc. IEEE Eur. Conf. Opt. Commun.*, Gothenburg, Sweden, Sep. 2017, pp. 1–3, Paper Th.PDP.A.3, doi: [10.1109/ECOC.2017.8346084](https://doi.org/10.1109/ECOC.2017.8346084).
- [11] F. Hamaoka *et al.*, "Ultra-wideband WDM transmission in S-, C-, and L-Bands using signal power optimization scheme," *J. Lightw. Technol.*, vol. 37, no. 8, pp. 1764–1771, Apr. 2019, doi: [10.1109/JLT.2019.2894827](https://doi.org/10.1109/JLT.2019.2894827).
- [12] L. Galdino *et al.*, "Optical fibre capacity optimisation via continuous bandwidth amplification and geometric shaping," *IEEE Photon. Technol. Lett.*, vol. 32, no. 17, pp. 1021–1024, Sep. 2020, doi: [10.1109/LPT.2020.3007591](https://doi.org/10.1109/LPT.2020.3007591).
- [13] B. J. Putnam *et al.*, "S, and extended L-Band transmission with doped fiber and distributed raman amplification," in *Proc. IEEE/OSA Opt. Fiber Commun. Conf. Exhib.*, Jun. 2021, pp. 1–3, Paper Th4C.2, [Online]. Available: ieeexplore.ieee.org/document/9489895
- [14] R. Elschner *et al.*, "Improving achievable information rates of 64-GBd PDM-64QAM by nonlinear transmitter predistortion," in *Proc. IEEE/OSA Opt. Fiber Commun. Conf. Exhib.*, San Diego, USA, pp. 1–3, Mar. 2018, Paper M1C.2, doi: [10.1364/OFC.2018.M1C.2](https://doi.org/10.1364/OFC.2018.M1C.2).

- [15] T. Duthel *et al.*, "Characterization and pre-distortion of linear and nonlinear transmitter impairments for PM-64QAM applications," in *Proc. VDE Eur. Conf. Opt. Commun.*, Dusseldorf, Germany, Sep. 2016, pp. 1–3, Paper W.4.P1.SC3.25, [Online]. Available: ieeexplore.ieee.org/document/7767721
- [16] R. Emmerich *et al.*, "S-band transmission with off-the-shelf C-band components enabled by nonlinear predistortion based on coherent system identification," in *Proc. VDE Photon. Netw.; 22th ITG-Symp., ITG-Fb.* vol. 297, Photonische Netze, May 2021, pp. 77–83, [Online]. Available: ieeexplore.ieee.org/document/9472219
- [17] M. Sena, R. Emmerich, B. Shariati, J. K. Fischer, and R. Freund, "Evaluation of an autonomous digital predistortion scheme for optical multiband systems," in *Proc. IEEE/OPTICA Opt. Fiber Commun. Conf. Exhib.*, San Francisco, CA, USA, Jun. 2021, pp. 1–3, Paper F4D.5, [Online]. Available: ieeexplore.ieee.org/document/9490011
- [18] M. Nölle *et al.*, "Characterization and linearization of high bandwidth integrated optical transmitter modules," in *Proc. IEEE Eur. Conf. Opt. Commun.*, Brussels, Belgium, pp. 1–4, Dec. 2020, Paper Tu2D-4, doi: [10.1109/ECOC48923.2020.9333184](https://doi.org/10.1109/ECOC48923.2020.9333184).
- [19] M. Selmi, Y. Jaouen, and P. Ciblat, "Accurate digital frequency offset estimator for coherent polmux QAM transmission systems," in *Proc. IEEE Eur. Conf. Opt. Commun.*, Vienna, Austria, Sep. 2009, pp. 1–2, Paper P3.08, [Online]. Available: ieeexplore.ieee.org/document/5287372
- [20] B. Szafraniec, B. Nebendahl, and T. Marshall, "Polarization demultiplexing in Stokes space," *Opt. Exp.*, vol. 18, no. 17, pp. 17928–17939, Aug. 2010, doi: [10.1364/OE.18.017928](https://doi.org/10.1364/OE.18.017928).
- [21] T. Pfau, S. Hoffmann, and R. Noe, "Hardware-efficient coherent digital receiver concept with feedforward carrier recovery for M-QAM constellations," *J. Lightw. Technol.*, vol. 27, no. 8, pp. 989–999, Apr. 2009, doi: [10.1109/JLT.2008.2010511](https://doi.org/10.1109/JLT.2008.2010511).
- [22] R. D. Nowak, "Penalized least squares estimation of volterra filters and higher order statistics," *IEEE Trans. Signal Process.*, vol. 46, no. 2, pp. 419–428, Feb. 1998, doi: [10.1109/78.655426](https://doi.org/10.1109/78.655426).
- [23] C. Eun and E. J. Powers, "A new volterra predistorter based on the indirect learning architecture," *IEEE Trans. Signal Process.*, vol. 45, no. 1, pp. 223–227, Jan. 1997, doi: [10.1109/78.552219](https://doi.org/10.1109/78.552219).
- [24] P. W. Berenguer *et al.*, "Nonlinear digital Pre-distortion of transmitter components," *J. Lightw. Technol.*, vol. 34, no. 8, pp. 1739–1745, Apr. 2016, doi: [10.1109/JLT.2015.2510962](https://doi.org/10.1109/JLT.2015.2510962).
- [25] R. Elschnner *et al.*, "Experimental demonstration of a format-flexible single carrier coherent receiver using data-aided digital signal processing," *Opt. Exp.*, vol. 20, no. 27, pp. 28786–28791, Dec. 2012, doi: [10.1364/OE.20.028786](https://doi.org/10.1364/OE.20.028786).
- [26] C. R. S. Fludger and T. Kupfer, "Transmitter impairment mitigation and monitoring for high baud-rate, high order modulation systems," in *Proc. VDE Eur. Conf. Opt. Commun.*, Dusseldorf, Germany, Sep. 2016, pp. 1–3, Paper Tu.2.A, [Online]. Available: ieeexplore.ieee.org/document/7767545
- [27] ITU-T, "G.698.2 : Amplified multichannel dense wavelength division multiplexing applications with single channel optical interfaces," in *Int. Telecommun. Union*, Nov. 2018, G.698.2(11/18), pp. 1–48, [Online]. Available: itu.int/rec/T-REC-G.698.2-201811-I

Robert Emmerich was born in Meiningen, Germany, in 1982. He received the B. Eng. degree in telecommunication engineering from the University of Applied Sciences HTW-Berlin, Berlin, Germany, in 2013, and the M.Sc. degree in electrical engineering from the Technische Universität Berlin, Berlin, Germany, in 2015. Since 2016, he has been a Research Associate with the Fraunhofer Institute for Telecommunications, Heinrich-Hertz-Institute, Berlin. His research interests include application of multiband transmission systems with higher order modulation and broadband digital coherent receivers and transmitters, where he is working toward the Ph.D. degree.

Matheus Sena received the B.Sc. and M.Sc. degrees in electrical engineering from the Federal University of Pernambuco, Recife, Brazil, in 2016 and 2018, respectively. He is working toward the Ph.D. degree with the Technische Universität Berlin, Berlin, Germany. In 2014, he was with the Polytechnic School of Engineering of New York University, New York, USA. Since 2019, he has been a Research Associate with the Fraunhofer Institute for Telecommunications, Heinrich-Hertz-Institute, Berlin. His research interests include cognitive transponders, pre-compensation techniques, multiband transmission systems and application of machine learning algorithms in optical communications.

Robert Elschnner (Member, IEEE) received the Dipl.-Ing. and Dr.-Ing. degrees in electrical engineering from Technische Universität Berlin, Berlin, Germany, in 2006 and 2011, respectively. In 2005, he was with École Nationale Supérieure des Télécommunications, Paris, France. Since 2010, he has been a member of the scientific staff and Project Manager with Fraunhofer Heinrich-Hertz-Institute, Berlin. His research interests include digital signal processing and nonlinear optics. Dr. Elschnner is a member of the IEEE Photonics Society and is currently the Technical Program Committee of the Optical Fiber Communication Conference.

Carsten Schmidt-Langhorst was born in Berlin, Germany, in 1972. He received the Dipl.-Phys. and the Dr. rer. nat. degrees in physics from the Technische Universität Berlin, Berlin, Germany, in 1997 and 2004, respectively. Since 1998, he has been with the Fraunhofer Institute for Telecommunications, Heinrich-Hertz-Institute, Berlin, Germany. Initially, he has been engaged in research on ultrafast fiber transmission and optical signal processing including all-optical sampling techniques. He is currently a member of scientific staff and Project Manager in the field of digital coherent optical transmission technology. He was the Technical Program Committee of the Optical Fiber Communication Conference. He was the recipient of the Philip Morris Research Award in 1999. Dr. Schmidt-Langhorst is a member of the Verband der Elektrotechnik Elektronik Informationstechnik (VDE) and the Deutsche Physikalische Gesellschaft (DPG).

Isaac Sackey received the B.Sc. degree in electrical and electronic engineering from the Kwame Nkrumah University of Science and Technology, Kumasi, Ghana, in 2002, the M.Sc. degree in electronics engineering from the Bremen University of Applied Sciences, Bremen, Germany, in 2010, and the Dr.-Ing. degree in electrical engineering from the Technische Universität Berlin, Berlin, Germany, in 2016. From July 2003 to January 2009, he worked with Hospital Engineering Limited, Accra, Ghana, as an Electronic Engineer. Since 2011, he has been working with the Sub-marine and Core Systems Group, the Fraunhofer Institute for Telecommunications, Heinrich-Hertz-Institute in Berlin, Germany. His research interests include parametric processes in nonlinear materials and coherent transmission in long-haul, metro-haul and short reach systems.

Colja Schubert received the Dipl.-Phys. and Dr. rer. nat. degrees in physics from Technische Universität Berlin, Berlin, Germany, in 1998 and 2004, respectively. He was Exchange Student with Strathclyde University in Glasgow, U.K., from 1996 to 1997. During his Dipl. thesis from 1997 to 1998, he was with Max-Born-Institute for Nonlinear Optics and Short Pulse Spectroscopy, Berlin, Germany. Since 2000, he has been a member of the scientific staff with Heinrich-Hertz-Institute, Berlin. His research interests include high-speed transmission systems and all-optical signal processing. He is currently Heading the Submarine and Core Systems Group with the Photonic Networks & Systems Department. Dr. Schubert is a member of the German Physical Society.

Ronald Freund received the Dipl.-Ing. and Dr.-Ing. degrees in electrical engineering from the Technical University of Ilmenau, Ilmenau, Germany, in 1993 and 2002, respectively, and the MBA degree from RWTH Aachen University, Aachen, Germany. In 1997, he Co-Founded VPI Systems Inc., where he was involved in as a Chief Technology Officer and Consultant, responsible for the development of design software for the physical layer of photonic networks. Since 1995, he has been with Heinrich Hertz Institute, Berlin, Germany, where he is currently Leading the Department of Photonic Networks and Systems. In 2017 he has been appointed as a Professor of photonic communication systems with the Technical University of Berlin, Berlin, Germany. He has authored or coauthored more than 150 scientific publications.